Automatic Detection and Classification of High-Frequency Oscillations in Depth-EEG Signals

Nisrine Jrad, Amar Kachenoura*, Isabelle Merlet, Fabrice Bartolomei, Anca Nica, Arnaud Biraben, and Fabrice Wendling

Abstract—*Goal*: **Interictal high-frequency oscillations (HFOs [30–600 Hz]) have proven to be relevant biomarkers in epilepsy. In this paper, four categories of HFOs are considered: Gamma ([30–80 Hz]), high-gamma ([80–120 Hz]), ripples ([120–250 Hz]), and fast-ripples ([250–600 Hz]). A universal detector of the four types of HFOs is proposed. It has the advantages of 1) classifying HFOs, and thus, being robust to inter and intrasubject variability; 2) rejecting artefacts, thus being specific.** *Methods*: **Gabor atoms are tuned to cover the physiological bands. Gabor transform is then used to detect HFOs in intracerebral electroencephalography (iEEG) signals recorded in patients candidate to epilepsy surgery. To extract relevant features, energy ratios, along with event duration, are investigated. Discriminant ratios are optimized so as to maximize among the four types of HFOs and artefacts. A multiclass support vector machine (SVM) is used to classify detected events. Pseudoreal signals are simulated to measure the performance of the method when the ground truth is known.** *Results*: **Experiments are conducted on simulated and on human iEEG signals. The proposed method shows high performance in terms of sensitivity and false discovery rate.** *Conclusion*: **The methods have the advantages of detecting and discriminating all types of HFOs as well as avoiding false detections caused by artefacts.** *Significance*: **Experimental results show the feasibility of a robust and universal detector.**

Index Terms—**Epilepsy, Gabor filters, interictal high-frequency oscillations (HFOs), intracerebral electroencephalography (iEEG), signal classification, signal detection, support vector machines (SVM).**

I. INTRODUCTION

FOR many patients with drug-resistant epilepsy, surgical resection represents the best therapeutic solution. Recently, a number of studies reported that interictal high-frequency oscillations (HFOs [30–600 Hz]) are reliable biomarkers of the epileptogenic zone [2]–[4]. In human, HFOs can be observed in intracerebral electroencephalographic (iEEG) signals recorded with multicontact depth electrodes. HFOs are nonstationary oscillations of low amplitude with various frequencies, morphologies, underlying pathophysiological mechanisms, and clinical significance. Studies often divided HFOs into two classes according to their frequency extent: Ripples (Rs [80–200 Hz]) and fast ripples (FRs [200–600 Hz]) [1], [5], [6]. Other research studies included gamma [7], [8] (γ [30–80 Hz]), and high-gamma [8], [9] (Hγ [80–120 Hz]) to the HFOs range. Consequently, HFOs can be categorized into four subbands [10]. Typical examples are shown in Fig. 1. HFOs may occur between seizures, at seizure onset, and during seizures. Interictal HFOs share similar spectral [11] and spatial characteristics [12] with ictal HFOs. As compared with interictal epileptic spikes (IES), the resection of brain structures generating interictal HFOs was shown to be correlated with more favorable surgical outcome [13].

In this context, the accurate detection and classification of interictal HFOs is a fundamental–but challenging–issue. Indeed, because of the inherent properties of HFOs, the automatic detection is not trivial. First, HFOs are short-duration (a few tens of ms) nonstationary transient events of low amplitude reflecting various mechanisms in underlying neuronal circuits. Second, iEEG recordings are often contaminated with environmental and physiological artefacts. Third, the bandpass filtering of transient signals, such as sharp waves and IES, leads to wrong detections [14]. Fourth, HFOs disclose wide morphological and spectral diversity caused by the intra and intersubject variabilities.

The objective of this study is to propose a versatile detector that accounts the diversity of HFOs and a robust one to the false detection. The basic principle is to use Gabor atoms to decom-
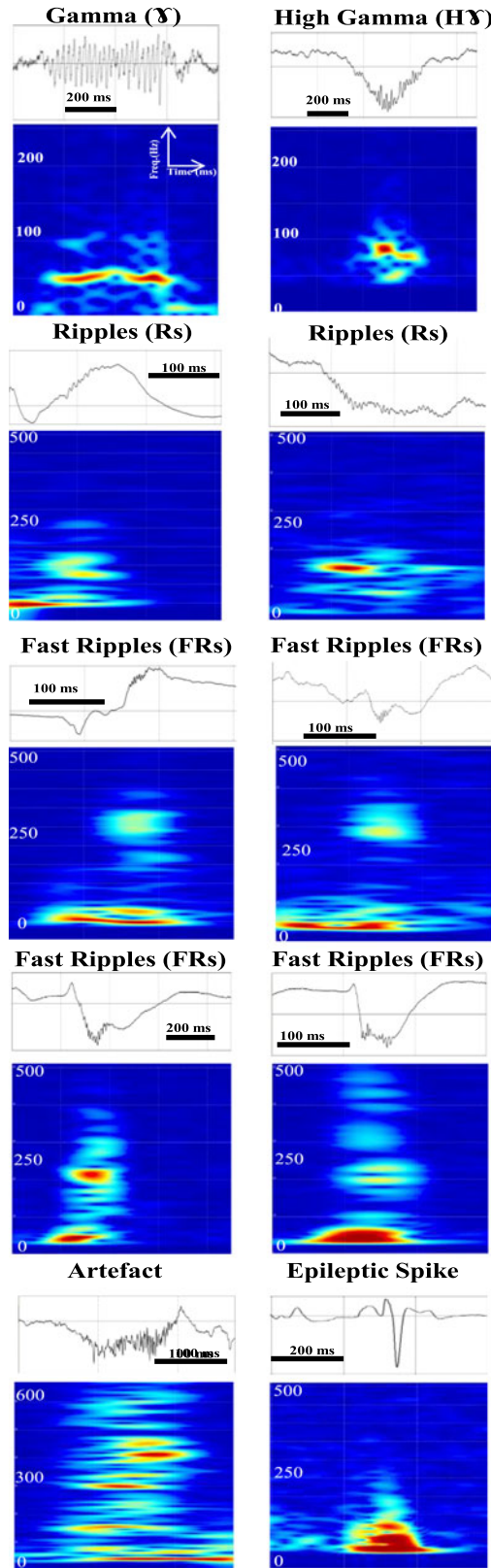
Fig. 1. Time and time–frequency representations of the four categories of HFOs (γ, Hγ, Rs, FRs), and misleading events (artefact, epileptic spike). These illustrations show the wide diversity of HFOs at the temporal and spectral levels. They also show the similarity between artefacts and HFOs.

pose the signal into subband signals contributing to the human physiological frequency bands. Gabor atoms were chosen due to their optimality regarding the time–frequency (T–F) uncertainty principle [15]. Duration and threshold criteria were applied on energy computed at the HFOs bands [30–600 Hz] to delineate the onset and offset of detected oscillations. Feature vectors were then extracted from the detections as a combination of energy ratio features [16]–[18] and temporal feature. A multi-class support vector machines (SVM) was used to classify detected events and label them: As one of the four different HFOs types; γ [30–80 Hz], Hγ [80–120 Hz], Rs [120–250 Hz], and FRs [250–600 Hz]; or as a high-frequency artefact (ART/IES). A comparison of the proposed method to a widely used detector [1], on large simulated and real datasets (6903 HFOs), demonstrates the high performance of our method. Besides, results promise the feasibility of a versatile detector/classifier able to adapt to the inter and intrasubject variability.

II. BACKGROUND

In early studies, detection of HFOs was first performed visually [5]. This is known to be a time consuming, very subjective, marginally consistent, and nonreproducible task. To cope up with these drawbacks, automated methods were proposed in the early 2000 [1]. State-of-the-art methods consisted of at least two of the following steps: Preprocessing, detection, feature extraction, classification, and artefact rejection. The preprocessing step was usually done by bandpass filtering the signal in the frequency band of interest (i.e., Rs and FRs bands in [1] and [19], respectively, and γ band in [7]) by using either a finite or infinite impulse response filter. In addition to filtering, Gardner *et al.* [7] proposed to whiten signal, using a first-order backward differencing filter. The detection step was based on thresholding energy in the time or the T–F domain and may include additional duration, amplitude, or waveform criteria. Early methods studied HFOs in the T–F domain [1], [7], [19]. Preprocessed signals were used to compute energy on a sliding window. Different energy forms were used such as L2-norm in [1], L1-norm in [7], or Hilbert envelope in [19]. Both amplitude and duration thresholds were used to characterize HFOs. Recently, the T–F domain has been explored [20], [21]. Typically, in [20], the T–F space was parametrized to search for bumps and bursts. HFO detectors were often of high sensitivity but suffered from moderate to poor specificity. Transients, with high energy, lead to false detection. For instance, sharp waves were usually considered as FRs. To reduce false detection, a solution was given based on binary classification such as in [16] and more recently in [22]. To classify detected events, discriminant features were extracted. Statistical features such as number of extrema, number of peaks, [22], frequential features [23], Fisher discriminant features [24], and spectral-based features [6] were used. The classification step exploited supervised methods for instance SVM [22], neural networks [25], decision trees [23], and k-nearest neighbors [24]. In addition, an unsupervised method based on k-medoids [6] was proposed. Other solutions were also used to enhance the detector specificity. For example, in [26], detected HFOs occurring simultaneously with

detected events on the reference electrodes were considered as artefacts and thus rejected.

To the best of our knowledge, the classification of HFOs was limited to the Rs+FRs bands. None of the previous methods did consider the whole band of HFOs (from gamma to fast ripples). This paper addresses the HFO multiclass detection and classification problem and differs from previous studies that limited their scope to one or two categories of HFOs. The main contributions of this paper are twofold. First, on the methodological level, T–F localization was optimized, in the sense of Heisenberg–Gabor uncertainty principle, using Gabor atoms [15], [27]. Rather than computing energy on a bandpass filtered signal, Gabor atoms were tuned so as to decompose the signal into its contribution in the physiological bands. Moreover, discriminant features were extracted to classify detections. Energy ratios show good discrimination ability in our previous work [16]–[18], and thus, they were exploited and combined to temporal feature. Second, on the experimental level, pseudoreal signals were simulated and used, along with the human signals, to assess the performance of the method. The main advantage of considering simulated signals is having a complete knowledge of their content: Time occurrence of transient events, type of events, and the ability to control the event to background ratio (EBR). Besides, the method was successfully validated on real iEEG signals.

III. MATERIALS

In this study, simulated data were used to assess the performance of proposed method on iEEG signals in which the ground truth is available (type of HFOs, occurrence times, EBR). Human iEEG signals were also studied to evaluate the method performance on iEEG recorded during presurgical evaluation of patients.

A. Human Signals

iEEG signals from five patients suffering from drug-resistant epilepsy were recorded in the Neurology Department of the University Hospital of Rennes, France. This monitoring was part of the usual presurgical clinical evaluation of patients and aimed at delineating epileptogenic and functionally preserved brain areas. All patients gave informed consent for participation in research studies. iEEG was recorded by using a 256-channel Brain Quick (Micromed, Italy) recording system with a sampling rate of 2048 Hz. No hardware filter was used in the acquisition procedure, except the high-pass filter with 0.1 Hz as a cutoff frequency classically used to remove the offset of the baseline. Intracerebral electrodes were composed of 8 to 18 cylindrical contacts (DIXI Microdeep electrodes, length: 2 mm, diameter: 0.8 mm, 1.5 mm apart, platine–iridium).

The visual annotation was done with Amadeus [28], an EEG reviewing software developed at LTSI, University of Rennes 1. HFO events were visually annotated by two reviewers independently. First, all electrodes were included in the visual screening. There was no *a priori* selection of electrode contacts according to explored regions, patient's state (awake/sleep), or quality of recordings. Second, electrodes showing visible HFOs, on the

ongoing background activity, were kept. Note that the goal of our paper was neither to detect exhaustively all HFOs nor to assess their relationship to the epileptogenic zone, but rather to obtain a representative database containing a sufficient number of HFOs to assess the detector performance on real and simulated data. Raw iEEGs were reviewed to make sure that no false detection (introduced by filtering) was included. Time resolution was increased to 1 s/page (to enhance visual inspection of low-amplitude oscillations) and up to 12 electrodes were visualized simultaneously. Each selected event was labeled as γ, Hγ, Rs, FRs or IES. IESs were considered because they often lead to false detection. Each event was systematically bandpass filtered (according to the HFOs frequency bands) to confirm the visual selection made on raw data. T–F analysis (spectrogram) was also used to check selected events. Around 3 h (times 12 electrodes) of recordings, resulting on 2200 min were reviewed. A total number of 6903 events were visually labeled. Four categories of events were visually detected and labeled as γ rhythm (1724 events), Hγ rhythm (1085 events), Rs (2019 events), and FRs (1476 events). Some IES (599 events) were also identified. It is worth mentioning that, to the best of the experts' knowledge, visually detected events were quite representative of HFOs.

To illustrate the wide diversity of this database, representative examples of the four HFOs classes, and that of artefact and IES are given in Fig. 1. Raw signals illustrate the temporal extent; which is variable, generally short for FRs and more extended for γ oscillations. The mean (standard deviation) values of the time duration are around 618 (349) ms for γ, 387 (161) ms for Hγ, 82 (39) ms for Rs, 69 (27) ms for FRs, and 130 (35) ms for IES. Time–frequency representations show the frequency location of the signal energy; which characterizes each type of rhythm. Artefacts (ART) and IESs disclose broadband energy in high-frequency bands and are thus source of wrong detections in the case where detection only relies on high-pass filtering. It is noteworthy that, for this dataset, many FRs have energy in both [120–250 Hz] and [250–600 Hz] frequency bands. More details about the neuropathologies of patients, clinical and neuroimaging information, and sites of recording are provided in the Supplementary materials.

B. Simulated Signals

The use of simulated signals allowed us to assess the method performance in a situation where the ground truth is known. To this end, real transient events (γ, Hγ, Rs FRs, and IES), extracted from iEEG signals of patients described above, were inserted into background activity. This background activity, was generated by using a computational model of neuronal population, analogous to a local field potential, and was shown to well approximate the background found in human iEEG recordings [27]. To avoid any discontinuity between the inserted real signal and the surrounding simulated signal, smoothing functions (sigmoids) were used at each transition Fig. 2(a). Sigmoid weights controlled the background activity level. An "EBR" was defined to adjust the event amplitude with respect to the background activity level. Events occurred randomly in the simulated signal, according to Poisson's law. The mean occurrence of events was
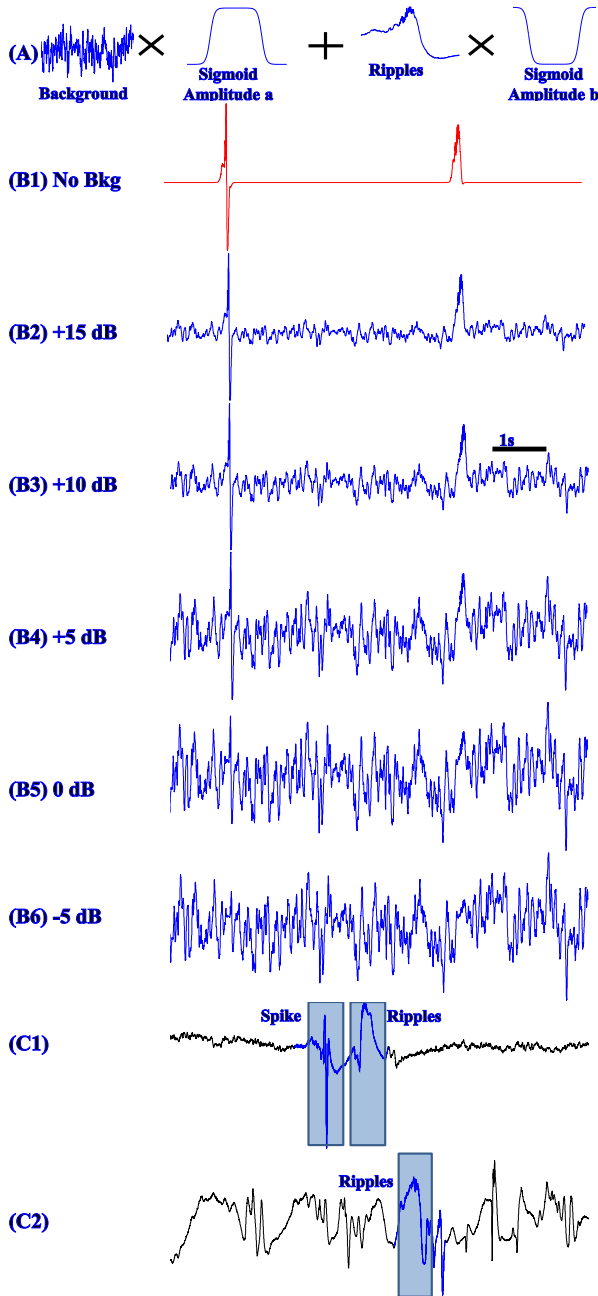
Fig. 2. Generation of simulated iEEG signals. (a) events (IES and Rs in the illustrated case) extracted from real iEEG were inserted in the simulated background activity. The background level was controlled and quantified by the EBR. Examples of 5.5 s simulated iEEG including an IES followed by an Rs for: (b1) EBR = infinity, (b2) EBR = +15 dB, (b3) EBR = +10 dB, (b4) EBR = +5 dB, (b5) EBR = 0 dB, (b6) EBR = −5 dB. (c1) is a 5.5 s of a patient's recordings showing an IES followed by an Rs oscillation. Note that events of the simulated signals, illustrated in this figure, were extracted from this patient iEEG. (c2) is another real signal example showing an iEEG with higher background amplitude than that of (c1).

set to 30/min. Five signals of 4 h were simulated with an average of 30 events/min. The EBR of signals was increased from −5 to +15 dB with a step of 5 dB. Examples are illustrated in Fig. 2. A short segment of 5.5 s simulated signal [see Fig. 2(b2)–(b6)] is shown with an IES inserted at $t = 0.75$ s followed by an Rs os-

cillation at $t = 3.75$ s. For high EBR (greater than 0 dB), both events appear clearly. In contrast, events can be hardly discriminated from background and are almost not visible for low EBR (≤0 dB). In order to compare simulated signals to real ones, a 5.5 s segment of two patients' recordings are also illustrated in Fig. 2(c1)—(c2). Simulated signals above 0 dB looks very representative of the real one. Note that Fig. 2(c1) is the one from which events of simulated signals were extracted.

IV. METHODS

The proposed method proceeded according to two steps: Detection and classification. As illustrated above, signals to be analyzed have specific features in frequency (frequency band) and in time (duration). This consideration led us to develop a *T–F* approach based on Gabor functions. These functions were chosen for their optimality regarding the Heisenberg–Gabor uncertainty principle [15], [27]: The minimal product of spatial and spectral supports is achieved by using a modulated Gaussian.

A. Problem Statement

Let $s(t)$ denote the iEEG signal in which high-frequency events will be detected. This signal essentially contains background activity where transient events appear randomly. Typically, these events are the HFOs (γ, Hγ, Rs, and FRs) and some other high-frequency artefacts, such as IES. The problem, addressed in this paper, consists of detecting these transient events, whatever the oscillation is, and then classifying them into five different classes, namely γ, Hγ, Rs, FRs, and ART/IES. In other words, the classifier should be able to discriminate among the four types of HFOs and any false detection (labeled as ART/IES in the sequel). We assume that an event, $x_m(t)$, $m = \{1, \ldots, M\}$, detected from the iEEG signal is characterized by its finite time support of length equal $\Delta t_m = t_m^{(\text{off})} - t_m^{(\text{on})}$, with M the total number of detected events, $t_m^{(\text{on})}$ and $t_m^{(\text{off})}$ are the onset and the offset boundary limit markers of the event. The entire set of detected events was written as $\{(x_1(t), y_1), \ldots, (x_m(t), y_m), \ldots, (x_M(t), y_M)\}$ with class labels $y_m \in \{'\gamma', '\text{H}\gamma', '\text{Rs}', '\text{FRs}', '\text{ART/IES}'\}$.

B. Automatic Detection and Classification

The proposed detector comprises two major stages (see Fig. 3). In the first stage, events of interest (EoIs) were detected. EoIs included the four types of HFOs along with any other false detection showing an energy increase in the high-frequency bands. This step was optimized so as to guarantee a good tradeoff between missed and false detections. In the second stage, signal features were extracted from the EoIs and were used as inputs to a classifier for automatic labeling. The objective of this step was twofold: To reduce the false alarm rate (by classifying false detections as ART/IES) and to categorize HFOs.

1) Detection of EoIs: Most HFOs detection methods used *T–F* methods to decompose iEEG signals. Unfortunately, most *T–F* approaches suffer from the limit of jointly improving time and frequency localizations. Indeed, for a good analysis of a signal, a narrow-window support is needed in both spatial
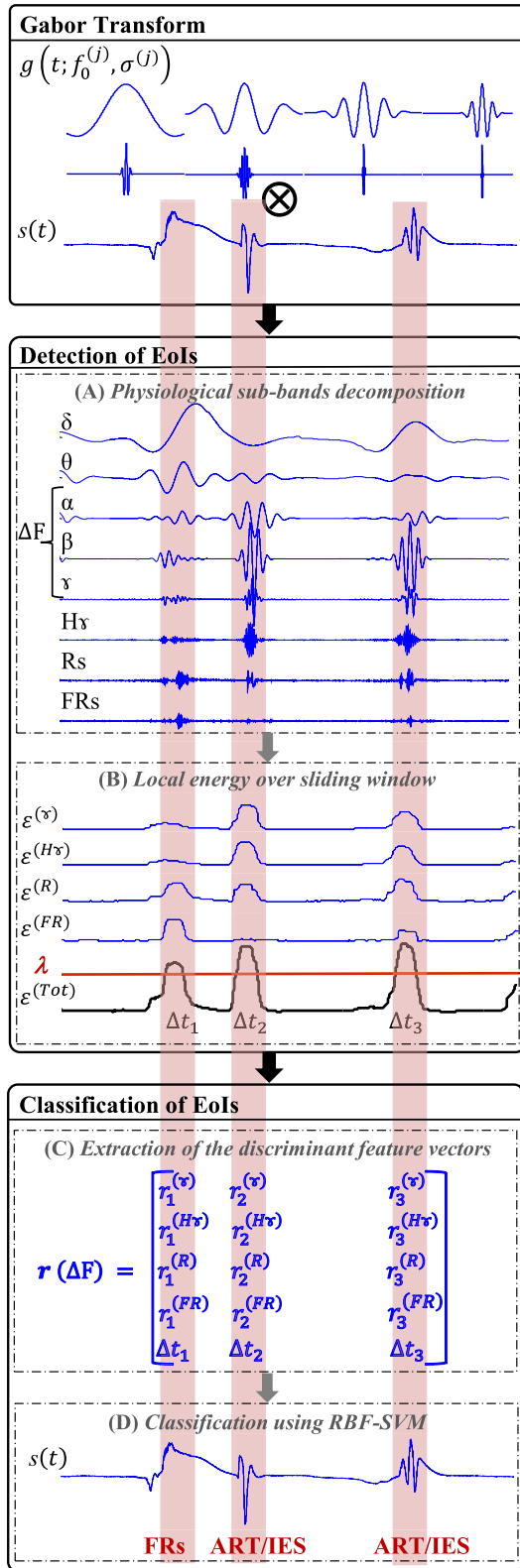
Fig. 3. Pipeline of the method: (a) Raw signal is decomposed, using Gabor atoms, into its contribution in the physiological bands; (b) Detection: EoIs are detected by thresholding the total energy, which is the sum of energies in γ, Hγ, Rs, and FRs bands; (c) discriminant features are extracted from the detected events. They consist of spectral characteristics (energy in γ, Hγ, Rs, and FRs normalized by the energy in the low-frequency bands) and temporal feature (event duration); (d) multiclass SVM is used to label detected EoIs.

and spectral domains. However, the product of spatial and spectral supports of an arbitrary window has a lower bound (refer to Heisenberg–Gabor uncertainty principle [27] for more details). Gabor demonstrated that a modulated Gaussian achieves this lower bound [15], [27]. The Gabor function is defined as a Gaussian envelope modulated by complex sinusoids

$$g\left(t; f_0, \sigma\right) = \frac{1}{\sqrt{2\pi}\sigma} e^{-\frac{t^2}{2\sigma^2}} e^{j2\pi f_0 t} \tag{1}$$

where the frequency f_0 centers the modulated Gaussian and the scale parameter σ sets its sharpness. The scale parameter defines also the extent of Gabor function, since it determines its rate of convergence toward zero. The Fourier transform of $g(t; f_0, \sigma)$ is a Gaussian function centered on f_0, and with a bandwidth inversely proportional to σ. It is given by

$$G\left(f; f_0, \sigma\right) = e^{-2\sigma^2\pi^2(f-f_0)^2}. \tag{2}$$

The Gabor transform of raw iEEG signals is given by convoluting the signal $s(t)$ and the Gabor function

$$c\left(t; f_0, \sigma\right) = s\left(t\right) * g\left(t; f_0, \sigma\right) = \sum_{i=-\infty}^{\infty} s\left(i\right) g\left(t-i; f_0, \sigma\right). \tag{3}$$

Although the convolution goes from minus infinity to infinity, the local neighborhood of the Gabor transform is defined by the Gaussian envelope.

In practice, as shown in Fig. 3(a), we used the Gabor transform to decompose the raw iEEG signals, $s(t)$, into its contributions in a frequency band j delineated by the parameters $f_0^{(j)}$ and $\sigma^{(j)}$ with $j \in \{\delta, \theta, \alpha, \beta, \gamma, \text{H}\gamma, \text{Rs}, \text{FRs}\}$ physiological bands. These bands include low frequencies (LF): δ [0.5–3.5 Hz], θ [3.5–8 Hz], α [8–15 Hz], β [15–30 Hz], and high frequencies (HF): γ [30–80 Hz], Hγ [80–120 Hz], Rs [120–250 Hz], FRs [250–600 Hz]. The parameters $f_0^{(j)}$ and $\sigma^{(j)}$ were precisely tuned in order to construct a set of Gabor functions, with spectral representation covering physiological bands.

After decomposing the iEEG signal $s(t)$, the local energy, at each frequency band of interest γ, Hγ, Rs, and FRs was computed over a sliding rectangular window of width N denoted by $w_N(t)$. The Gabor root mean square (RMS) energy is written as

$$\varepsilon^{(j)}\left(t\right) = \sqrt{\frac{1}{N} \sum_i \left(c\left(i; f_0^{(j)}, \sigma^{(j)}\right)\right)^2 w_N\left(i-t\right)}. \tag{4}$$

The detection was done according to the total RMS energy at HFOs bands, which is computed as the sum of RMS energies, (4), in the γ, Hγ, Rs, and FRs bands

$$\varepsilon^{(\text{Tot})}\left(t\right) = \sum_{j=\gamma}^{\text{FRs}} \varepsilon^{(j)}\left(t\right). \tag{5}$$

The RMS empirical cumulative distribution function (CDF) of the entire signal was computed and an optimal threshold λ (percentile of the CDF) was set as a good breakpoint between HFOs and false detections. Successive RMS segments with amplitudes above λ, and longer than $\Delta t_m = t_m^{(\text{off})} - t_m^{(\text{on})} =$

6.5 ms in duration are detected and delineated by an onset and an offset boundary limit markers $t_m^{(\text{on})}$ and $t_m^{(\text{off})}$, respectively. Consecutive events less than 5 ms apart were grouped together and considered as the same event.

C. Classification of EoIs

In this stage, detected EoIs should be classified as $'\gamma'$, $'H\gamma'$, $'Rs'$, $'FRs'$ or $'ART/IES'$. To this end, discriminant features Fig. 3(c) were extracted from EoIs and used as the inputs to the radial basis function support vector machine (RBF-SVM) classifier. As shown in Fig. 1, transient events are characterized by their temporal and spectral extents. These characteristics were used to compute relevant features. Thus, for each detected EoI $x_p(t)$, energies in $'\gamma'$, $'H\gamma'$, $'Rs'$ and $'FRs'$ bands and the event duration $\Delta t_m = t_m^{(\text{off})} - t_m^{(\text{on})}$ were calculated. A five-dimensional feature vector was thus defined as

$$\boldsymbol{\varepsilon_m} = \left[\varepsilon_m^{(\gamma)} \ \varepsilon_m^{(H\gamma)} \ \varepsilon_m^{(R)} \ \varepsilon_m^{(\text{FR})} \ \Delta t_m \right]^T. \tag{6}$$

We had previously shown that the sole energy feature leads to poor performance when separating FRs from IES [16]–[18]. Therefore, in the present study, we introduced the energy ratio as a feature vector. The energy ratio of the mth event at a band j, is given by

$$r_m^{(j)}(\Delta f) = \frac{\varepsilon_m^{(j)}}{\sum_{k \in \Delta f} \varepsilon_m^{(k)}} \tag{7}$$

where Δf is the frequency band that maximizes the separation between the five classes of the detected EoIs. The new feature vector, based on energy ratios, is written as

$$\boldsymbol{r_m}(\Delta f) = \left[r_m^{(\gamma)}(\Delta f) \ r_m^{(H\gamma)}(\Delta f) \ r_m^{(R)}(\Delta f) \ r_m^{(\text{FR})}(\Delta f) \right.$$
$$\left. \Delta t_m \right]^T. \tag{8}$$

D. Performance Metrics

Since our method proceeded according to two stages, detection and classification, performance was first evaluated for each step, taken separately. Then, the global performance of the whole method was assessed.

1) Detection Level: The performance of the detector stage can be quantitatively analyzed using the receiver operating characteristic (ROC) curves. The ROC curve is a parametric plot representing sensitivity (Se) as a function of specificity (Sp), when varying threshold λ. Se is the proportion of detected events overlapping with visually detected events and Sp is the proportion of correctly rejecting the background. Se and Sp are commonly defined as follows:

$$\text{Se} = \frac{\text{True Positive}}{\text{Positive}} = \frac{\text{TP}}{\text{P}} \tag{9}$$

$$\text{Sp} = \frac{\text{True Negative}}{\text{Negative}} = \frac{\text{TN}}{\text{N}} \tag{10}$$

where *true positive* (TP) is the number of correctly detected HFOs, *positive* (P) is total number of visually detected HFOs,

true negative (TN) accounts for background activity correctly rejected by the detector, and *negative* (N) is the background activity. In our case, TN and N might be estimated as epochs of background, according to a chosen window size [29] (one negative sample will be defined as a background epoch). Given the large amount of TN data in HFOs detection task, ROC curves can be misleading. *Se-false discovery rate* (FDR) curve was hence preferred. FDR is defined as

$$\text{FDR} = \frac{\text{False Positive}}{\text{False Positive + True Positive}} = \frac{\text{FP}}{\text{FP + TP}} \tag{11}$$

where *false positive* (FP) is the number of wrongly detected HFOs, namely background and ART/IES. The FDR is a metric used to characterize the rate of misclassified events. The Se versus the FDR curve was then used to define the optimal threshold λ.

2) Classification Level: Classification performance was computed based on the detected EoIs and not on the entire set of EoIs. Hence, we evaluated the generalization ability of the classifier, whatever the detector performance is. In practice, Se and Sp were computed, according to (9) and (10), for each class $y_m \in \{'\gamma', 'H\gamma', 'Rs', 'FRs', 'ART/IES'\}$. For a given class y_m, TP are detected EoIs that are correctly classified, P is the total number of detected EoIs in class y_m, TN are the detected EoIs that are correctly rejected from y_m and N is the total number of detected EoIs that do not belong to y_m.

3) Detection and Classification Level: To evaluate the performance of the whole method (detection and classification), the global Se and FDR were computed as described on the detection level, with the difference that TP and FP were computed based on classified detections. In other terms, detected HFOs wrongly classified as ART/IES were not included in the TP of (9) and false detections correctly classified as ART/IES were not included in the FP of (11).

E. Parameters Optimization

The efficiency of the proposed procedure depends on the tuning of two main parameters: λ and Δf. For the detection step, threshold parameter λ was selected according to the operating point of the Se-FDR curve, among a set of values ranging from 0.8 to 0.99 (step of 0.005). Indeed, threshold value for which the corresponding Se-FDR curve point close to the best detector (Se 1, FDR 0) was retained. For the feature extraction, the energy band Δf is selected so as to maximize Se and Sp of the classes, which is analog to maximizing the accuracy of the classifier. Parameters were optimized on a training/validation sets and then used to compute performance on a blind testing set.

V. RESULTS

Three experiments were considered in this section to evaluate the proposed method. The objective of the first one was to evaluate the efficiency of the energy ratio and of the event duration as discriminant features for the five classes. The second experiment was performed on simulated datasets. Its aim was to assess the method performance when the occurrence time and the category of EoIs are known *a priori* (ground truth). In this

case, the robustness of the method to EBR could also be evaluated. The third experiment was conducted on human recordings to measure the efficiency of the method on real depth-EEG signals. Eventually, a comparative study with Staba's detector [1], on both simulated and real data, was performed.

A. Δf Band Optimization and Features Extraction

The objective of this experiment was to show the discrimination power of the proposed ratio $r_m(\Delta f)$ (8), when using the optimal Δf. To this end, the entire dataset described in Section III-A was considered. For each event, four different feature vectors were extracted as follows:

1) $fv1_m = r_m(\Delta f)$ is the energy ratio based feature vector, with the event duration Δt_m, defined in (8);
2) $fv2_m = [r_m^{(\gamma)}(\Delta f)\ r_m^{(H\gamma)}(\Delta f)\ r_m^{(R)}(\Delta f)\ r_m^{(FR)}(\Delta f)]^T$ is the same as $fv1_m$ without including the event duration Δt_m;
3) $fv3_m = \varepsilon_m$, is the energy-based feature vector, with the event duration Δt_m, defined in (6); and
4) $fv4_m = [\varepsilon_m^{(\gamma)}\ \varepsilon_m^{(H\gamma)}\ \varepsilon_m^{(R)}\ \varepsilon_m^{(FR)}]^T$ is the same as $fv3_m$ without including the event duration Δt_m.

The four vectors were tested and their relevance was compared in term of classification accuracy. More precisely, the whole dataset was resampled, using a five-cross validation, into training, validation and testing sets on a per class basis. Training set was used to learn SVM for different values of kernel parameter (for each feature vector). Besides, for $fv1_m$ and $fv2_m$, 16 different values of Δf were tested: [0.5–3.5], [0.5–8], [0.5–15], [0.5–30], [0.5–80], [3.5–8], [3.5–15], [3.5–30], [3.5–80], [8–15], [8–30], [8–80], [15–30], [15–80], [30–600], [0.5–600] Hz. Validation set was used to select the optimal kernel parameter and the optimal Δf. Finally, the performance was computed in terms of Se and Sp on the blind testing set (as detailed in Section IV-D2).

Fig. 4 illustrates Se and Sp boxplots of γ, Hγ, Rs, FRs, and ART/IES classes computed using the four feature vectors $fv1_m$, $fv2_m$, $fv3_m$, and $fv4_m$, respectively. It shows that the new Gabor ratio feature vector computed in the band $\Delta f = [8$—80 Hz] and combined with the event duration, $fv1_m$, led to the best Se and Sp, for all events. The Se and Sp obtained by using $fv1_m$ and $fv2_m$ were better than those obtained for $fv3_m$ and $fv4_m$, respectively, especially for Rs and FRs. This finding corroborated our previous studies [16]–[18] showing that energy features cannot discriminate between FRs and ART/IES. Even if the results obtained using only the energy-ratio vector $fv2_m$ were very interesting, the exploitation of the event duration Δt_m improved Se and Sp of all classes, especially that of Rs, FRs, and ART/IES.

A detailed analysis of the results was achieved by computing confusion matrices on the four different feature vectors (see Table I). This revealed that the feature vectors, $fv1_m$ and $fv2_m$, based on energy ratios [see Table I(a) and (b)] eliminated almost all the incorrect predictions (off-diagonal elements) found on energy-based classification [see Table I(c) and (d)]. In particular, confusions between (ART/IES, Rs) and (ART/IES, FRs) were completely removed, which is very im-
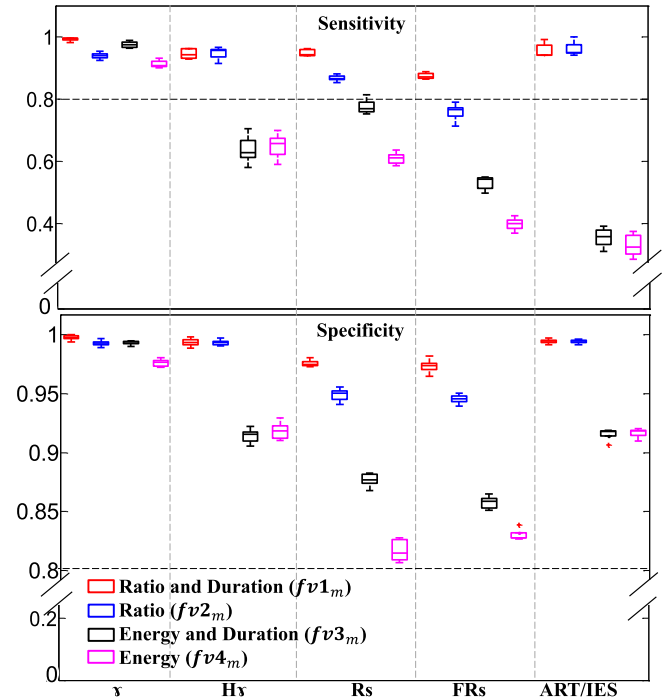

Fig. 4. Sensitivity and specificity boxplots computed on a test set of the five classes. Red boxes give the performance of the classifier by using energy ratio and temporal features. Blue boxes show performance computed on energy ratio features. Black boxes are performance based on energy and time features. Pink boxes illustrate performance computed on energy features.

portant since it improved the Se of the detector (no more false alarms will be introduced after classification of detected EoIs). Moreover, including event durations to energy ratio features reduced the confusion among close classes as reported in Table I(a). It is noteworthy that, even in the best case where $fv1_m$ was used, 32 of 288 FRs were still wrongly classified as Rs. This could be explained by the fact that FRs may also display energy in the Rs frequency band (as shown in Fig. 1).

In the sequel, in agreement with the results of this first experiment, energy ratio, and duration feature vector $fv1_m$ computed in the band $\Delta f = [8 - 80\ \text{Hz}]$ and the optimal kernel parameter will be retained as optimal settings for classification.

B. Simulated Data

Simulated data consisted in five signals of four hours each, with an average of 30 events/min, when varying the EBR from -5 to $+15$ dB by step of 5 dB. Note that, in our simulations, the percentage of ART/IES was set to 17%. iEEG signals were divided into a training set (70% of iEEG duration) and a testing set (30% of the iEEG duration). Training set was used to learn a detector (Gabor-based or Staba's detector) as well as the SVM classifier. Then, the stability of methods was assessed on blind testing sets, which does not include the training set.

Using Se-FDR curves, the training consists of selecting the optimal parameter(s): Threshold λ for the proposed Gabor detector and two standard deviations for Staba's detector, defining

TABLE I
CONFUSION MATRICES

(a)

Predicted/True	γ	Hγ	Rs	FRs	ART
γ	**278**	6	0	0	0
Hγ	0	**195**	6	3	0
Rs	0	6	**387**	32	7
FRs	1	0	0	**256**	0
ART	1	3	11	4	**113**

(b)

Predicted/True	γ	Hγ	Rs	FRs	ART
γ	267	3	16	31	0
Hγ	0	192	17	7	1
Rs	3	10	356	25	5
FRs	10	2	3	226	0
ART	0	3	12	6	114

(c)

Predicted/True	γ	Hγ	Rs	FRs	ART
γ	277	55	10	3	0
Hγ	0	148	68	3	0
Rs	2	5	304	119	35
FRs	1	1	14	161	44
ART	0	1	8	9	41

(d)

Predicted/True	γ	Hγ	Rs	FRs	ART
γ	261	48	55	88	33
Hγ	0	147	77	9	1
Rs	1	3	247	70	13
FRs	18	9	15	120	36
ART	0	3	10	8	37

Confusion matrices computed on: (a) Energy ratio and duration features, (b) energy ratio features, (c) energy and duration features, and (d) energy features. Columns represent the true classes (γ, Hγ, Rs, FRs, and ART/IES), and rows represent the classifier prediction.

Fig. 5. Se-FDR curve computed on the training set for the +10 dB simulated data for γ, Hγ, Rs, and FRs. On the top (a): Se-FDR curves of the Gabor-based proposed detector. On the bottom (b): Se-FDR curves of Staba's detector.

TABLE II
PERFORMANCE ON SIMULATED DATA

EBR	Performance measures	Se	FDR
+15	Detection	0.947(0.007)	0.178(0.009)
	Detection and Classification	0.924(0.008)	0.036(0.007)
	Staba *et al.* [1]	0.898(0.014)	0.188(0.016)
+10	Detection	0.937(0.003)	0.185(0.005)
	Detection and Classification	0.916 (0.007)	0.037(0.002)
	Staba *et al.* [1]	0.846(0.029)	0.206(0.029)
+5	Detection	0.838(0.017)	0.199(0.006)
	Detection and Classification	0.818(0.017)	0.039(0.001)
	Staba *et al.* [1]	0.638(0.016)	0.257(0.025)
0	Detection	0.575 (0.049)	0.269 (0.040)
	Detection and Classification	0.555(0.052)	0.044(0.017)
	Staba *et al.* [1]	0.070(0.011)	0.731(0.038)
−5	Detection	0.362(0.009)	0.237(0.028)
	Detection and Classification	0.295(0.009)	0.027(0.003)
	Staba *et al.* [1]	0.000(0.000)	0.998(0.001)

Simulated data: Performance measures on test set for different EBR. Se and FDR are computed before classification where artefacts are not rejected, and after classification to measure the role of the classifier enhancing the specificity of the overall detection. Se and FDR of Staba's detector [1] are also given for comparison.

the energy threshold, and the rectified data threshold (see [1] for more details). Indeed, parameters value for which the corresponding Se-FDR curve point is close to the top left corner (Se 1, FDR 0) was selected. Fig. 5 illustrates Se-FDR curves computed on the +10 dB simulated signals for both Gabor-based and Staba methods. Se-FDR curves clearly showed that Gabor-based detector outperformed Staba's one.

The performance of the whole method (including both detection and classification) on test signals was reported in Table II as the mean and standard deviation of Se and FDR. The performance computed for the detection stage by using Gabor detector without classification and Staba's detector were also reported in this table. Noteworthily, Staba's detector did not propose a classification step. Results showed globally a very good performance of the proposed method. When compared to Staba's detector, the Gabor-based detector and the whole detection and classification method gave better performance in terms of Se and FDR. This finding was inline with results computed on the training sets.

To illustrate the behavior of our method, we reported results in the case of EBR = +10 dB, where 1382 HFOs and 283 ART/IES were inse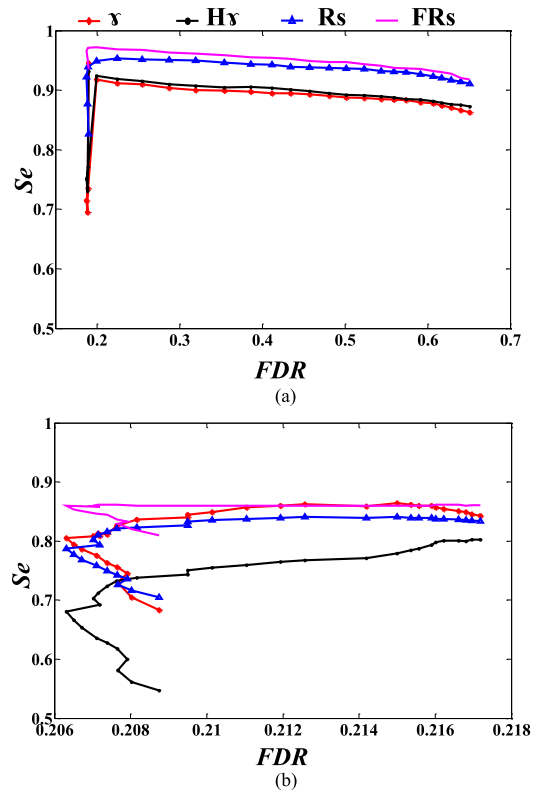rted into the test signals. The whole method succeeded in well classifying 1258 HFOs with only 36 false detections. For all EBR, FDR decreased drastically after classification to reach less than 0.04. Interestingly, this decrease illustrated the amount of wrong detections that were rejected by the classifier (correctly categorized as ART/IES). The classification stage helped rejecting false detections at the price of a small loss of Se. At most, Se decreased of 2%, except

TABLE III
PERFORMANCE ON SIMULATED DATA

EBR	γ		Hγ		Rs		FRs		ART/IES	
	Se	Sp	Se	Sp	Se	Sp	Se	Sp	Se	Sp
+15	0.994 (0.003)	0.998 (0.001)	0.975 (0.012)	0.989 (0.002)	0.822 (0.009)	0.912 (0.007)	0.735 (0.007)	0.984 (0.001)	0.958 (0.015)	0.965 (0.002)
+10	0.997 (0.003)	0.999 (0.000)	0.981 (0.006)	0.990 (0.002)	0.816 (0.020)	0.914 (0.012)	0.745 (0.027)	0.982 (0.002)	0.9478 (0.010)	0.967 (0.001)
+5	0.992 (0.004)	0.997 (0.001)	0.982 (0.006)	0.983 (0.002)	0.787 (0.020)	0.928 (0.012)	0.773 (0.039)	0.986 (0.002)	0.935 (0.013)	0.971 (0.003)
0	0.984 (0.006)	0.995 (0.002)	0.986 (0.009)	0.959 (0.011)	0.611 (0.092)	0.956 (0.005)	0.820 (0.020)	0.985 (0.004)	0.869 (0.030)	0.972 (0.008)
−5	0.989 (0.005)	0.993 (0.005)	0.991 (0.006)	0.948 (0.015)	0.600 (0.076)	0.978 (0.005)	0.769 (0.184)	0.991 (0.005)	0.770 (0.054)	0.987 (0.007)

Simulated data: Performance measures of test signals. Mean (standard deviation) of sensitivity and specificity are reported for the five classes and for different EBR.

for a −5 dB EBR where the loss was of 6.7%. Note that, for EBR = −5 dB and EBR = 0 dB, events were visually undetectable and the amplitude of background activity was prominent as compared to that of EoIs. In that case, the performance of the method decreased.

To make sure that there was no confusion when classifying the different types of HFOs, the performance of the classifier on detected EoIs was detailed in Table III. Mean and standard deviation of Se and Sp were computed on detected EoIs of the test signals for different EBR. For all EBR the Se and Sp were high, which means that the SVM classifier correctly categorized the detected EoIs. Regarding the positive EBR, classification performance of detected EoIs was in line with those shown in Section V-A: The same classification confusion between Rs and FRs as those seen in Table I(a) appeared in Table III. Indeed, Se of FRs was around 0.745 and Sp of Rs was around 0.914. This means that some FRs were wrongly classified as Rs.

C. Real Data

As for simulated data, real iEEG signals were divided into a training set (70% of iEEG) and a testing set (30% of iEEG). The training set was used to select the threshold λ on a Se-FDR curve. The SVM was constructed, using the optimal settings, on visually detected events that did not belong to the patient under study. The test set was used to compute the performance of the whole automatic detector and classifier on a blind set. Performance was computed on the basis of HFOs type. The clinical reviews were considered as the ground truth.

Mean and standard deviation of performance (given in Table IV) showed the good performance of the method. Indeed, Se of the detector was high: of at least 0.853 (0.056) for the detection stage and 0.746 (0.171) after the classification stage. The FDR was high when we only considered the detection stage. This clearly reflected that iEEG signals were highly contaminated with artefacts and emphasized the need of classifying the detected EoIs. The classification step led to a huge decrease of FDR: for instance, it diminished of 36.8% for γ. This decrease showed the amount of wrong detections that were rejected by the classifier (correctly categorized as ART/IES). In addition, the classification stage did not hamper the efficiency of the detector in term of Se that decreased of around 5% for γ and Hγ. This decrease revealed that around 5% of γ or Hγ were mainly categorized as ART/IES. Regarding Se decrease for Rs and FRs, they were slightly more pronounced than that of γ and

TABLE IV
PERFORMANCE ON REAL DATA

HFOs	Performance measures	Se	FDR
γ	Detection	0.926 (0.021)	0.523 (0.007)
	Detection and Classification	0.872 (0.041)	0.155 (0.019)
	Staba *et al.* [1]	0.887(0.007)	0.552(0.008)
Hγ	Detection	0.853 (0.056)	0.428 (0.164)
	Detection and Classification	0.798 (0.111)	0.306 (0.122)
	Staba *et al.* [1]	0.624(0.031)	0.743(0.208)
Rs	Detection	0.918 (0.112)	0.600 (0.309)
	Detection and Classification	0.811 (0.188)	0.302 (0.155)
	Staba *et al.* [1]	0.850(0.191)	0.624(0.279)
FRs	Detection	0.961 (0.019)	0.247 (0.192)
	Detection and Classification	0.746 (0.171)	0.063 (0.017)
	Staba *et al.* [1]	0.755(0.214)	0.330(0.123)

Real data: Performance measures on test set. FDR are computed before classification where artefacts are not rejected, and after classification to measure the role of the classifier enhancing the specificity of the overall detection. Se and FDR of Staba's detector [1] are also given for comparison.

Hγ. This loss corroborated with the results obtained on simulated data where we reported confusion between Rs and FRs classes (mainly FRs misclassified as Rs). To prove this claim, we provided the performance of the classifier on detected Rs and FRs. Se was of 0.917 (0.008) for Rs and 0.728 (0.111) for FRs while Sp was of 0.738 (0.159) for Rs and 0.933 (0.094) for FRs. Finally, when comparing to Staba's detector, results were consistent with those found on simulated data. Indeed, the proposed detector (standalone) and detector/classifier method showed higher Se and lower FDR than Staba's ones.

VI. DISCUSSION

We presented here a robust and universal detector that detects and classifies the different types of HFOs with a high Se and a low FDR. It is validated on simulated data. It shows consistent performance on a group of patients and displays coherent performance on simulated and real data. This detector is simple to implement and run, and essentially requires the tuning of one parameter, the threshold λ. It is clinically helpful and easy to use.

On the methodological level, the use of Gabor functions is very adequate due to their optimality at the sense of Heisenberg Gabor uncertainty principle. Moreover, the fact that HFOs duration is inversely proportional to their frequency content (as seen in Section III) makes the use of Gabor very suitable. In-

deed, Gabor temporal support is also inversely proportional to its spectral extent.

An original point of this study is the use of realistic simulated data, which provides a ground truth on both the occurrence time and the type of events. It is important to note that these simulated signals mimicked real iEEG recordings. Another utility of these simulations is that they allowed measuring the robustness of the method when the background is predominant. In this study, a neural mass model was used to generate physiologically-plausible background activity [30] in which real HFOs (recorded in patients with depth-EEG electrodes) were inserted. In its current form, this model cannot be directly tuned to generate transient activity in the [200–600 Hz] frequency band. However, we are currently developing a model at similar level (mesoscopic, neural field) to simulate HFOs generated in the cerebral cortex and observed on depth-EEG electrode contacts [31].

So far, no research addressed the diversity of HFOs and how to classify them into four rhythms while rejecting false detections at the same time. As compared to other studies that tackled artefact rejection as a tool to reduce the FDR and enhance the specificity, the proposed method is very competitive. For instance, in [20], a decision tree approach ensured a low FDR = 8.62% of FRs at the expense of a big loss in Se (Se reached 66.96%). For our method, even though the classification stage led to an average Se loss of 10%, it drastically decreased the FDR with an average of 24%. These findings seem to be in line with results of [26], where authors reported a 10% of loss of Se and a 28.7% of decrease of FPR (FPR = 1 − Sp). Nevertheless, it is noteworthy that FDR is a more general measure than FPR. FDR includes all kinds of false detections whereas FPR is based on visually detected artefacts and does not include any other wrong detected transients. In [6], Blanco *et al.* proposed Gaussian mixture models (GMM)-based method to reject detected events similar to background. A k-medoids algorithm was then used to cluster remaining detected events into Rs, FRs, Rs+FRs, or artefacts. This method seems effective, although no performance metrics were reported. However, its implementation is much more demanding than the one, we proposed in terms of complexity and time. In addition, although the classifier was presented as unsupervised, the GMM step required a training set, which means that the detection method is not completely unsupervised.

All the results obtained in our study show that the proposed method presented good performance (high Se and low FDR). The majority of actual HFOs, whether they are inserted in simulated background activity or visually detected on real data, were correctly detected and classified. It is noteworthy that it is more difficult to visually detect FRs than γ oscillations, especially for low EBR, since the amplitude of FRs is lower than the amplitude of γ oscillations. This may create a slight unavoidable bias in the reported performance. A key finding of our study is the low FDR. Indeed, energy ratio features, combined with event duration, reveal a big discriminant ability to categorize the four HFOs classes and to separate them from artefacts. Moreover, performance is consistent on all signals, showing that the method is robust to intra and intersubject variability. For the optimum
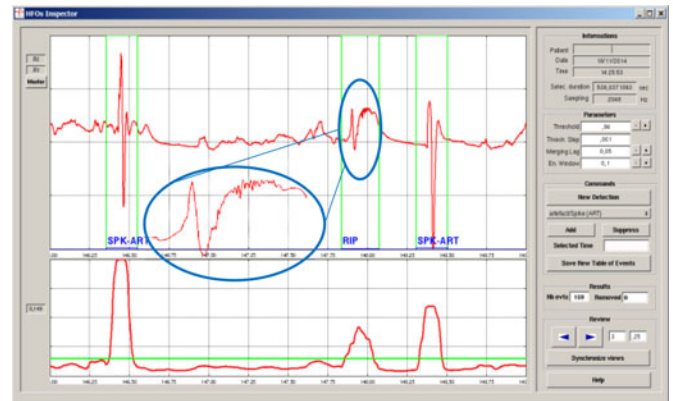

Fig. 6. Implementation of the proposed detector in user-friendly software designed to inspect detection results and test different parameters, if needed. The user selects in Amadeus the electrode he wants to analyze (upper view). A segment of about 536 s of B2-B3 is selected. The sliding energy and the threshold (0.149) appear in the lower view. Automatically detected onset and offset markers along with the label of classes appear in the upper view.

threshold, Se of real and simulated data is very similar whereas FDR of real data are higher than those computed on simulated data before and after the classification stage. This can be explained by the fact that automatic detector may find true HFOs that were missed by experts, and hence, considered as a false detection while computing the performance. Indeed, experts often miss some clear events, especially the unclear and doubtful ones.

Another key point of the proposed method is its limited number of parameters to be tuned. Among all parameters, the energy threshold λ is the most crucial one. Although considering a set of thresholds, one for each single frequency band, may lead to increased sensitivity, a unique threshold computed over all frequency bands of interest was privileged. Indeed, considering a set of thresholds increases FDR and processing time making its benefit questionable. It is important to mention that the threshold λ was set as the percentage of the energy CDF giving a good compromise between HFOs and false detections. This assumes that a population of HFO events is indeed present in the signal, which may not be the case. Fortunately, the classification step is added to help reducing the impact of this shortcoming. Indeed, non-HFOs detections will be mostly labelled as artefacts.

Finally, the proposed method is relatively easy to implement. A friendly graphical user interface (GUI) was developed to make it helpful for clinicians [32] (as can be seen in Fig. 6). This GUI allows the detection, selection, and validation of automatically and visually detected HFOs. We do believe that this implementation can dramatically reduce the workload and allow for reviewing a huge amount of interictal iEEG data recorded with dense iEEG systems (128–256) at high sampling rate (above 2 kHz). In the same purpose, several toolboxes were developed and evaluated as a means to detect HFOs [16], [33]–[37]. Moreover, a recent evaluation study developed four state of the art detection methods within a GUI application [38]. Despite the limitations they may have, these detectors assist clinicians and researchers in the identification of HFOs. Hence, it is of high

interest to consider them as useful tools to quantify the clinical yield of HFOs in a large variety of patients.

VII. CONCLUSION

Recent studies have showed a close relationship between brain regions producing interictal HFOs and those involved at seizure onset. This has motivated the development of an automatic detector. The major contribution of this paper was the proposition of a universal and accurate detector adapted to a wide diversity of HFOs. Detection was based on Gabor transform. Energy ratios and temporal features were extracted and classified according to a supervised SVM. The proposed method was universal, since it detected and discriminated all HFOs categories. Hence, it was robust to intra and intersubject variability. It was accurate, since it showed good and consistent performance on simulated and real datasets. The SVM classifier rejected artefacts, yielding low FDR. The results obtained so far are very promising and an extensive clinical validation will be conducted in future work. Another perspective will consider intermediate mixed classes, such as (Rs+FRs). Regarding the classification stage, it could be interesting to test unsupervised classifiers, since no unsupervised detection strategy has been proposed so far.

REFERENCES

[1] R. J. Staba *et al.*, "Quantitative analysis of high-frequency oscillations (80–500 Hz) recorded in human epileptic hippocampus and entorhinal cortex," *J. Neurophysiol.*, vol. 88, no. 4, pp. 1743–1752, Oct. 2002.

[2] M. Zijlmans *et al.*, "High-frequency oscillations as a new biomarker in epilepsy," *Ann. Neurol.*, vol. 71, no. 2, pp. 169–178, 2012.

[3] J. Jacobs *et al.*, "High-frequency oscillations (HFOs) in clinical epilepsy," *Progress Neurobiol.*, vol. 98, no. 3, pp. 302–315, 2012.

[4] J. Jacobs *et al.*, "Interictal high-frequency oscillations (80–500 Hz) are an indicator of seizure onset areas independent of spikes in the human epileptic brain," *Epilepsia*, vol. 49, no. 11, pp. 1893–1907, Nov. 2008.

[5] A. Bragin *et al.*, "High-frequency oscillations in human brain," *Hippocampus*, vol. 9, no. 2, pp. 137–142, 1999.

[6] J. A. Blanco *et al.*, "Unsupervised classification of high-frequency oscillations in human neocortical epilepsy and control patients," *J. Neurophysiol.*, vol. 104, no. 5, pp. 2900–2912, Nov. 2010.

[7] A. B. Gardner *et al.*, "Human and automated detection of high-frequency oscillations in clinical intracranial EEG recordings," *Clin. Neurophysiol.*, vol. 118, no. 5, pp. 1134–1143, May 2007.

[8] P. J. Uhlhaas *et al.*, "A new look at gamma? High- (>60 Hz) γ-band activity in cortical networks: Function, mechanisms and impairment," *Progress Biophys. Mol. Biol.*, vol. 105, no. 1–2, pp. 14–28, 2011.

[9] S.-C. Park *et al.*, "Ictal high-gamma oscillation (60–99 Hz) in intracranial electroencephalography and postoperative seizure outcome in neocortical epilepsy," *Clin. Neurophysiol.*, vol. 123, no. 6, pp. 1100–1110, 2012.

[10] J. G. R. Jefferys *et al.*, "Mechanisms of physiological and epileptic HFO generation," *Progress Neurobiol.*, vol. 98, no. 3, pp. 250–264, 2012.

[11] G. A. Worrell *et al.*, "High-frequency oscillations and seizure generation in neocortical epilepsy," *Brain*, vol. 127, pt 7, pp. 1496–1506, Jul. 2004.

[12] M. Zijlmans *et al.*, "Ictal and interictal high frequency oscillations in patients with focal epilepsy," *Clin Neurophysiol.*, vol. 122, no. 4, pp. 664–671, Apr. 2011.

[13] J. Jacobs *et al.*, "High-frequency electroencephalographic oscillations correlate with outcome of epilepsy surgery," *Ann Neurology*, vol. 67, no. 2, pp. 209–220, Feb. 2010.

[14] C. G. Benar *et al.*, "Pitfalls of high-pass filtering for detecting epileptic oscillations: a technical note on "false" ripples," *Clin. Neurophysiol.*, vol. 121, no. 3, pp. 301–310, Mar. 2010.

[15] D. Gabor, "Theory of communication," *J. Inst. Elect. Eng.*, vol. 93, no. 26, pp. 429–457, 1946.

[16] G. Birot *et al.*, "Automatic detection of fast ripples," *J. Neurosci. Methods*, vol. 213, no. 2, pp. 236–249, Mar. 15, 2013.

[17] N. Jrad *et al.*, "Gabor transform for interictal high frequency oscillations classification," in *Proc. Int. Conf. Adv. Biomed. Eng.*, 2015, pp. 127–130.

[18] N. Jrad *et al.*, "Classification of high frequency oscillations in epileptic intracerebral EEG," in *Proc. 37th Annu. Int. Conf. IEEE Eng. Med. Biol. Soc.*, 2015, pp. 574–577.

[19] B. Crepon *et al.*, "Mapping interictal oscillations greater than 200 Hz recorded with intracranial macroelectrodes in human epilepsy," *Brain*, vol. 133, pt. 1, pp. 33–45, Jan. 2010.

[20] S. Chaibi *et al.*, "A comparaison of methods for detection of high frequency oscillations (HFOs) in human intacerberal EEG recordings," *Amer. J. Signal Process.*, vol. 3, no. 2, pp. 25–34, 2013.

[21] S. Burnos *et al.*, "Human intracranial high frequency oscillations (HFOs) detected by automatic time-frequency analysis," *PLoS One*, vol. 9, no. 4, 2014, Art. no. e94381.

[22] M. Amiri *et al.*, "High frequency oscillations and spikes: Separating real HFOs from false oscillations," *Clin. Neurophysiol.*, vol. 127, no. 1, pp. 187–196, 2016.

[23] S. Chaibi *et al.*, "Detection of high frequency oscillations (HFOs) in the 80–500 Hz range in epilepsy recordings using decision tree analysis," in *Proc. 1st Int. Image Process., Appl. Syst. Conf.*, 2014, pp. 1–6.

[24] H. Firpi *et al.*, "High-frequency oscillations detected in epileptic networks using swarmed neural-network features," *Ann. Biomed. Eng.*, vol. 35, no. 9, pp. 1573–1584, 2007.

[25] M. Dümpelmann *et al.*, "Automatic 80–250 Hz "ripple" high frequency oscillation detection in invasive subdural grid and strip recordings in epilepsy by a radial basis function neural network," *Clin. Neurophysiol.*, vol. 123, no. 9, pp. 1721–1731, 2012.

[26] S. V. Gliske *et al.*, "Universal automated high frequency oscillation detector for real-time, long term EEG," *Clin. Neurophysiol.*, vol. 127, pp. 1057–1066, 2015.

[27] P. Flandrin, *Time-Frequency/Time-Scale Analysis*. Orlando, FL, USA: Academic, 1998.

[28] F. Wendling, "Software Amadeus-Visualisation," INSERM-Université de Rennes 1, APP IDDN no.: FR.001.420017.000.S.P.2015.000.31230, 2015.

[29] C. D. Doshi, "*Methods for detecting high-frequency oscillations in ongoing brain signals: Application to the determination of epileptic seizure onset zones,*" M.S. thesis, Marquette Univ., Milwaukee, WI, USA, 2011.

[30] F. Wendling *et al.*, "Interictal to ictal transition in human temporal lobe epilepsy: Insights from a computational model of intracerebral EEG," *J. Clin. Neurophysiol.*, vol. 22, no. 5, pp. 343–356, 2005.

[31] P. B. M. Shamas *et al.*, "Computational modeling of high frequency oscillations recorded clinical intracranial macro-electrodes," in *Proc. 38th Annu. Int. Conf. Eng. Med. Biol. Soc.*, Orlando, FL, USA, 2016, pp. 1014–1017.

[32] N. Jrad *et al.*, "HFOLAB," INSERM-Université de Rennes 1, APP IDDN no.: FR.001.140012.000.S.P.2016.000.31230, 2016.

[33] S. Burnos *et al.*, "The morphology of high frequency oscillations (HFO) does not improve delineating the epileptogenic zone," *Clin. Neurophysiol.*, vol. 127, no. 4, pp. 2140–2148, 2016.

[34] M. Dümpelmann *et al.*, "Temporal and spatial characteristics of high frequency oscillations as a new biomarker in epilepsy," *Epilepsia*, vol. 56, no. 2, pp. 197–206, 2015.

[35] K. Kerber *et al.*, "Differentiation of specific ripple patterns helps to identify epileptogenic areas for surgical procedures," *Clin. Neurophysiol.*, vol. 125, no. 7, pp. 1339–1345, 2014.

[36] F. Melani *et al.*, "Continuous high frequency activity: A peculiar SEEG pattern related to specific brain regions," *Clin. Neurophysiol.*, vol. 124, no. 8, pp. 1507–1516, 2013.

[37] N. Roehri *et al.*, "Time-frequency strategies for increasing high-frequency oscillation detectability in intracerebral EEG," *IEEE Trans. Biomed Eng.*, vol. 63, no. 12, pp. 2595–2606, Dec. 2016.

[38] M. Navarrete *et al.*, "RIPPLELAB: A comprehensive application for the detection, analysis and classification of high frequency oscillations in electroencephalographic signals," *PLoS One*, vol. 11, no. 6, 2016, Art. no. e0158276.

Authors' photographs and biographies not available at the time of publication.